E-Journal of Advanced Maintenance Vol.14 No. 1 (2022) 01-11
Japan Society of Maintenology

Improved three-dimensional atom probe tomography procedures for analyzing irradiation-induced microstructures

Ba-Vu-Chinh NGUYEN[1,5,1]*, Kenta MURAKAMI[1,2,2]*, Liang CHEN[3], Phongsakorn PRAK TOM[4], and Xinrun CHEN[1]

[1] *Nagaoka University of Technology, 1603-1 Kamitomioka, Nagaoka City, Niigata 940-2188, Japan*
[2] *The University of Tokyo, 7 Chome-3-1 Hongo, Bunkyo City, Tokyo 113-8654, Japan*
[3] *SJTU Paris Elite Institute of Technology, Shanghai Jiao Tong University, Shanghai 200240, China*
[4] *Malaysian Nuclear Agency, Bangi, 43000 Kajang, Selangor, Malaysia*
[5] *University of Science and Education, The University of Danang, Danang 555700, Vietnam*

ABSTRACT

Three-dimensional atom probe tomography (APT) is an excellent technique for identifying nanometer-sized solute atom enrichment regions, but the relationship between these nano-features and crystal orientation has not been well analyzed, except for in some semiconductor materials. In this study, a method that combines crystal orientation analysis of field desorption map and geometrical calculations to improve the reconstruction parameters for APT analysis was applied. Spherical Cu-rich clusters and planar Mn and Ni segregations on dislocation loops in Fe model alloys after ion irradiation were used as indicators for this analysis. The matrix atoms were well reconstructed. In addition, Cu-enriched regions formed as discrete clusters, while Mn- and Ni-enriched regions tended to be connected as part of a torus. The Cu-rich clusters had an oval shape with the smaller dimension along the z-axis, which may be due to the difference in the field evaporation between Cu(I) and Fe(II). The orientations of some Mn and Ni segregations were found by analyzing the desorption images, proving the decoration on the edge of dislocation loops. The distribution of solute atoms in the iron lattice was consistent with previous studies, confirming the correctness of this method for analyzing minority elements distributed in metal alloys.

KEYWORDS

APT, solute atoms, dislocation loop, nano-features, crystal orientation.

ARTICLE INFORMATION

Article history:
Received 09 January 2022
Accepted 11 July 2022

1. Introduction

In light-water reactors, the properties of reactor pressure vessel (RPV) materials change after long time operation owing to fast neutron irradiation. Many studies have reported the hardening and embrittlement of RPV materials because of the formation of solute-rich precipitates, such as copper-rich precipitates (CRPs) or manganese–nickel precipitates (MNPs), as well as matrix defects, namely, interstitial dislocation loops [1][2][3][4][5][6]. In body-centered cubic (BCC) iron, interstitial dislocation loops with two types of Burger vector, 1/2<111> and <100>, have been investigated [7][8]. They may act as nucleation sites for solute atom aggregation and accelerate precipitation [9][10]. Because solute atoms tend to accumulate at the lattice defects, such as dislocation loops, under the effect of irradiation or thermal aging, some special planes enriched in minority elements might be produced [11][12]. In that case, the orientation of dislocation loops can be represented by the orientation of the enriched solute planes. By determining the orientation of these planes, the formation of solute precipitates, as well as the interaction between solute atoms and the dislocation loop, can be better understood and modeled. Structural changes at the microscopic level cause a change in the mechanical properties of the material. Current understanding of the degradation mechanism of RPV

1*Corresponding author, E-mail: nbvchinh@ued.udn.vn
2*Corresponding author, E-mail: murakami@n.t.u-tokyo.ac.jp

materials reveals that the formation of Mn-Ni-Si clusters in microstructure of RPV material is one of the major causes of irradiation induced hardening and embrittlement [13], and their segregation into dislocation loops may contribute to the nucleation of Mn-Ni-Si clusters [9]. Therefore, the direction of enriched solute planes is an important feature that must be studied to better model property changes in RPV materials.

The direction of the planes can be determined if the orientation of the main lattice structure of the specimen is known. The lattice distances in atom probe tomography (APT) images can be accurately determined for some pure metals and semiconductors that have a high purity and poles that are easily found in desorption images (DI) or clear lattice planes in the APT image [14][15][16]. In addition, a combination of different techniques can be used to obtain the orientation in the specimens. In multi-grains characterization, as described by Herbig el al. [12], transmission electron microscopy (TEM) and APT are applicable to investigate crystallographic information at the nanometer scale. A similar combination has also been carried out by Belkacemi et al. [17]. In their analysis using both TEM and APT data at the same area, the **g.b** = 0 invisible criterion was applied to determine Burger vectors of dislocation loops appeared in iron alloys, and the APT image was combined with electron backscattered diffraction (EBSD) patterns to identify the specific crystallographic orientation, and therefore, the solute enrichment plane. Combining multiple methods allows the calculation of the exact orientation of the distribution of the solute atoms as well as the orientation of the dislocation loop plane. However, it may be time consuming or have high technical requirements and other special requirements for machinery and equipment. For a metallic alloy, calculation of the orientation of nanometer-sized planes, particularly for irradiated samples, remains difficult using only APT because of several reasons. (1) Commercial RPV materials are strained owing to the steel-making process [18]. When the sample is miniaturized, the strain is released, and the sample becomes distorted, which can slightly change the crystallographic orientation of the top and bottom of the sample. (2) The reconstructed atom map may be distorted because differences in atomic size obscure the pole figure of the DI which is the basis of orientation analysis in APT [19]. (3) To increase the identification accuracy of trace elements, many APTs are equipped with a reflectron, which lengthens the ion flight path. Consequently, the number of poles that can be identified by DI may be reduced [20][21].
In APT analysis, there are many important reconstruction parameters that need to be considered, such as the image compression factor (ICF), the initial radius of the specimen needle tip (R), and the field factor (k). These parameters vary with both the instrument and specimen. In this paper, by carefully preparing specimens and selecting reconstruction parameters for APT, we propose a method that combines orientation analysis of the desorption map and geometrical analysis to identify nano-features of solute elements present in irradiated RPV model alloys.

2. Experiment

2.1. Materials

Before irradiation, the specimen surface was treated by mechanical as well as electrochemical polishing. The electrochemical polishing conditions were 60 V at 10 °C in an acidic solution containing 95% acetic acid and 5% perchloric acid for 10 s. Two RPV model alloys were prepared. The first specimen was ion-irradiated FeMnNi (1.4 wt.% Mn and 0.6 wt.% Ni), in which solute-enriched planes along <111> and <100> were expected. The irradiation condition was 2.8 MeV Fe^{2+} ions at 400 °C until an average dose of 2 dpa was reached. The other specimen was FeCu (1.0 wt.% Cu), in which spherical solute enrichment was expected. It was irradiated by 2.8 MeV Fe^{2+} ions at 300 °C for 1 dpa. The irradiation work was conducted at the High Fluence Irradiation Facility of the University of Tokyo [22]. Displacement damage of the sample was calculated by the stopping and range of ions in matter (SRIM – 2013) program [23] using 40 eV as the displacement energy. From the SRIM results, the appropriate depth for sampling specimens by focused ion beam (FIB) was determined.

2.2. Specimen Preparation

To ascertain the effect of crystallographic orientation on the measurements, specimens were lifted-out from multiple grains. Initially, the specimens were mounted onto the specimen coupon provided by the APT vendor (a Si substrate with micro-pillars for mounting the specimens). However, handling the thin and smooth coupons was difficult for the engineers in the radiation-controlled area. Therefore, to improve the measurement yield, we decided to use a tungsten needle with an electrochemically polished tip attached to a copper tube as a base on which to deposit the specimens.
Specimens with a triangular prism shape (2 µm sides and 1 µm height) were prepared using a Hitachi FB2200 FIB system at Nagaoka University of Technology. The raw specimen had four sides and was deposited by tungsten to ensure a good connection between the sample and needle tip holder.
The FIB processing was performed immediately before the APT measurement at the Fugen Decommissioning Engineering Center of the Japan Atomic Energy Agency (JAEA) to prepare the final specimen (diameter of several tens of nanometers) using a Hitachi NB5000 system.

2.3. APT Analysis

APT measurements were conducted using a LEAP 3000X HR (CAMECA) at the Fugen Decommissioning Engineering Center of the JAEA. The laser pulse mode was applied, in which the wavelength, pulse ratio, and pulse rate were 532 nm, 0.2, and 250 kHz, respectively. Specimens were maintained at a very low temperature (~38.4 K) to reduce the effect of the thermal vibration of atoms in the lattice during the evaporation process. The detection efficiency of this system was estimated to be 37%. The electric field was chosen to be close to the evaporation field of Fe^{2+} (33 V/nm), which was the primary element in the alloy.

3. Improvement of Reconstruction Procedures

3.1. Selection of the Region of Interest (ROI)

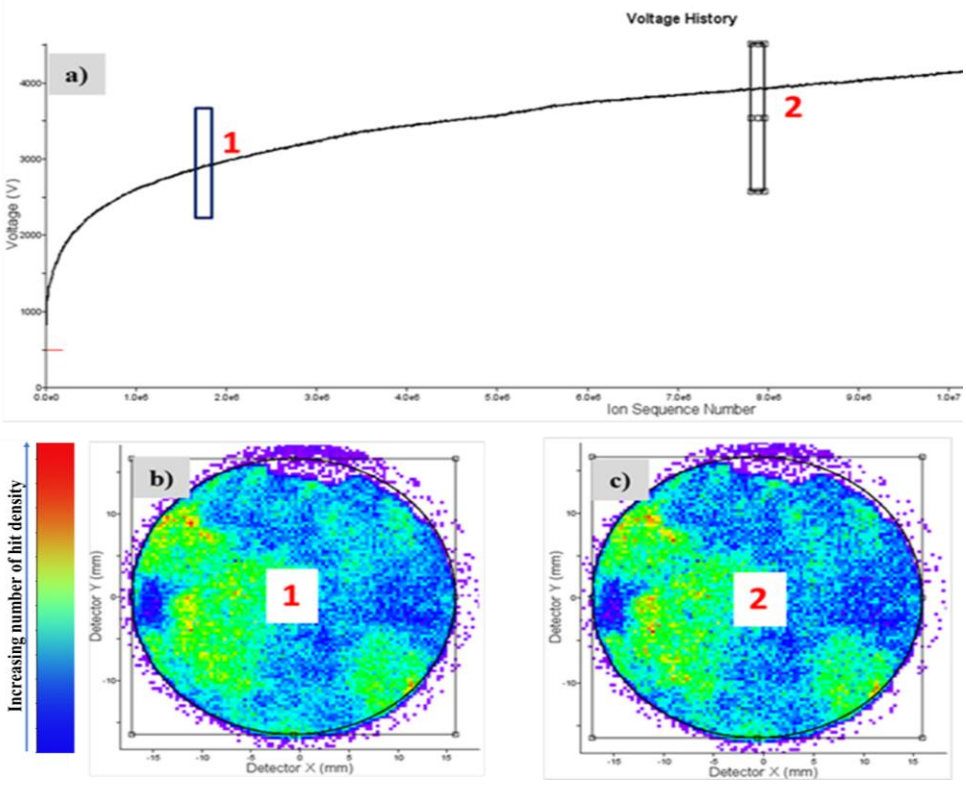

Fig. 1 – Information to be considered in setting the region for reconstruction. (a) Relationship between the total number of ions acquired and specimen voltage; the DI at the (b) top and (c) bottom of the specimen.

Reconstruction was performed using the Integrated Visualization and Analysis Software (IVAS, version 3.8). First, using the data shown in Fig. 1, the ROI for reconstruction was determined. Fig. 1a plots the change in the voltage applied to the specimen during a single APT analysis as a function of the number of acquired ions. Because the tip of the specimen was thin, a relatively low voltage was required for field evaporation, but as the specimen became thicker, the applied voltage increased. A sharp change in the voltage indicates the radius of the sample changes discontinuously, which may occur owing to a small fracture near the tip during the measurement. The detector hit map is a visualization of the integrated number of detected atoms at each position on the two-dimensional APT detector. Because the atomic positions are projected from the spherical surface of the sample to a flat detector, the detector hit map shows the polar points representing the crystal orientation of the sample. Changes in the pole figure at a certain position on the sample indicate that the crystal orientation of the sample with respect to the z-direction is changing at that location. In Fig. 1, the detector hit map does not change from the top to the bottom of the sample; therefore, it can be concluded that the entire sample can be reconstructed at once.

3.2. Image Compression Factor and Pole Figures

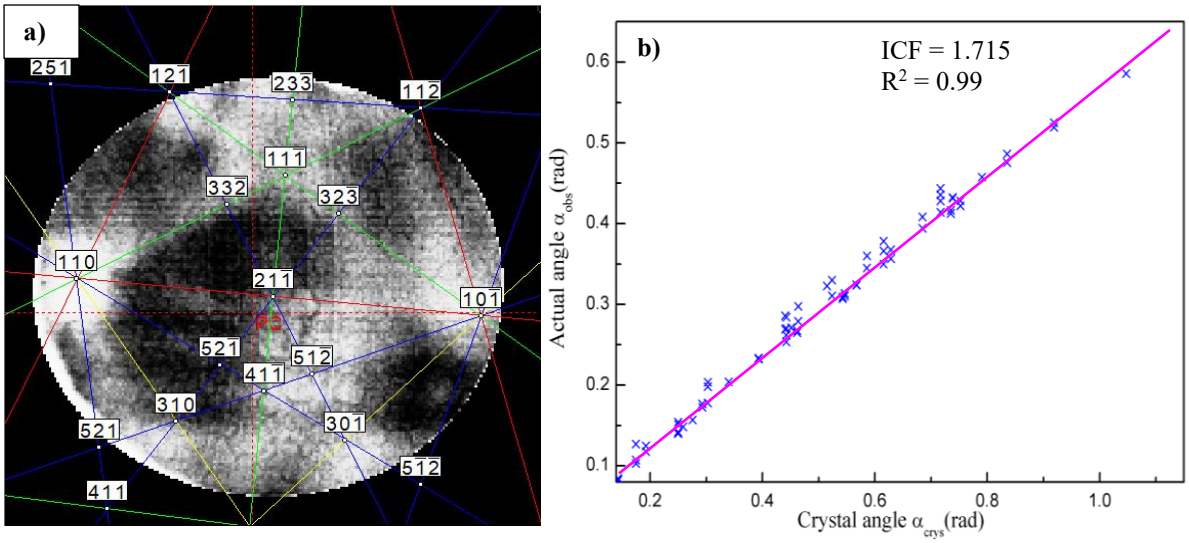

Fig. 2 – OIM analysis for determining the ICF value. The solution of index for the field desorption image was chosen for the highest index confidence and the lowest degree of mismatch [26]**. (a) Detection of poles. As shown here, the center of the detector is close to pole [21-1]; other poles are also observed. (b) Linear relationship between the observed and theoretical angles. The x- and y-axes are the crystal angle (α_{crys}) and observed angle (α_{obs}), respectively, and the ICF is the slope of the fitted line.**

Because of the deformation of the electric field lines around the apex of the needle tip, when an atom is ionized and evaporated from the needle tip, its trajectory is not a straight line. Therefore, the theoretical angle (α_{crys}) between two crystallographic directions and the observed angle (α_{obs}) obtained on the detector hit map differ. The ratio between the tangent of crystal angle α_{crys} and that of observed angle α_{obs} is named the image compression factor (ICF). In IVAS, using a low angle approximation, the ICF was automatically determined based on the linear relationship between the real (observed) angle and the theoretical (crystal) angle of the poles. After this process, the compression factor set by IVAS was relatively accurate. However, a slight deviation in the results remained due to the macroscopic heterogeneity of the specimen. To reduce this deviation, the following steps were applied to finalize the compression factor:

(1) Based on the DI, the Orientation Imaging Microscopy (OIM) function automatically generated several options of poles [24][25]. Considering for BCC structure and carefully comparing the recommended patterns with poles position and zone lines in the DI, we could select the best index solution (Fig. 2a). After this image processing, the distance from each (pole to pole) was measured. With the total number of active poles is n, the number of combinations of pole-to-pole distance pairs is:

$$N = \binom{n}{2} = \frac{n!}{2!\,(n-2)!} \qquad (1)$$

In the above formula, it is necessary to have a minimum of 2 poles to perform this calculation step. For instance, in Fig. 2a, number of active poles was n = 12, then N = 66 fitting points.

(2) According to the distance from the needle tip to the detector center, the flight path of an ion corresponding to each pole was calculated.

(3) Using the correlation between (1) and (2), the observed angle α_{obs} was estimated. The observed angle was the angle between the trajectory of the ions emitted from each surface of the sample and the normal of the detector.

(4) The crystal angle α_{crys} was obtained by calculating the nominal direction of the detector and the crystallographic tilt of each atomic plane.

(5) An approximately linear correlation between the observed angle and the crystal angle was expected for all fitting points. In Fig. 2b, every point in the graph corresponding to each (pole to pole) appeared in the detector. The slope of the correlation line was defined as the image compression factor: ICF $\approx \alpha_{crys}/\alpha_{obs}$.

3.3. Identification of the Initial Tip Radius

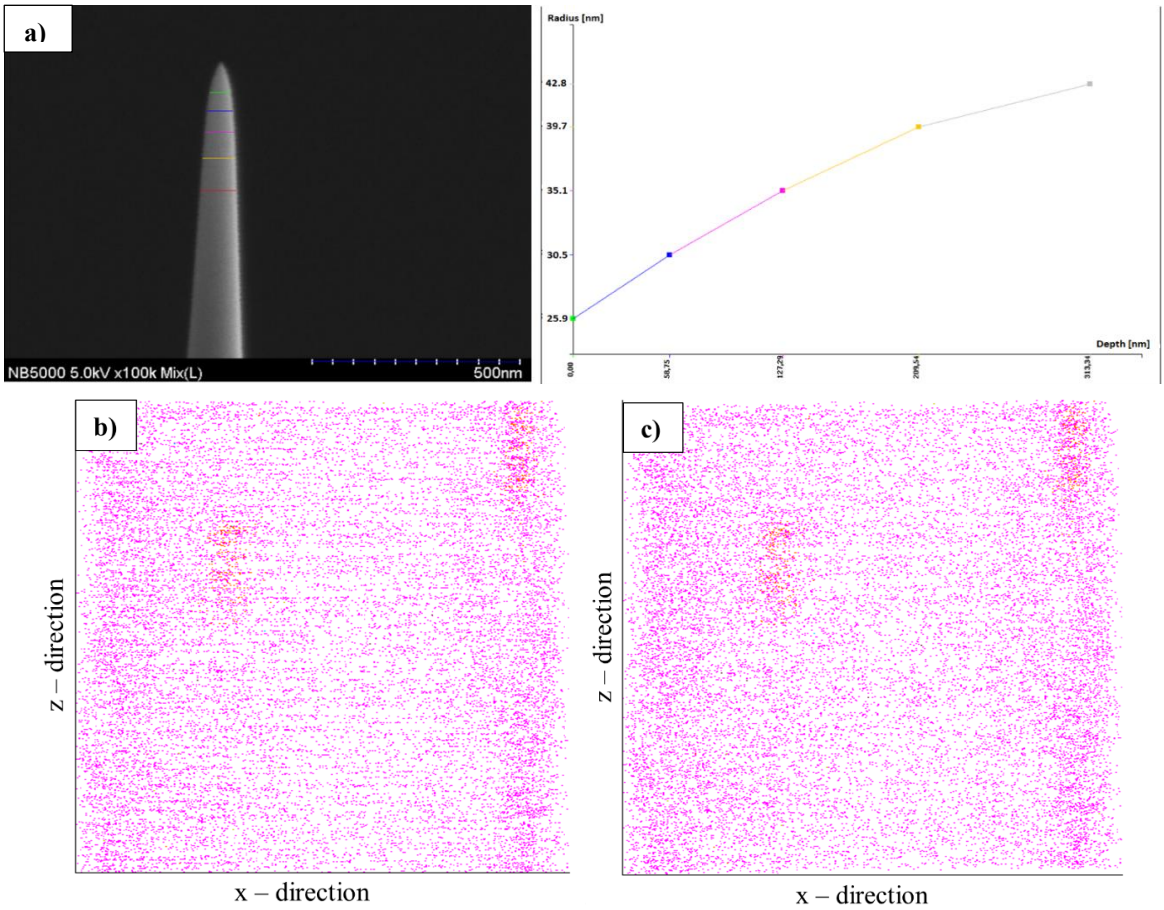

Fig. 3 – Estimation of tip radius. (a) Tip radius profile using SEM image. Radii at five different positions were automatically calculated based on the scale given by SEM image and fit the *k*-factor. (b) Good radius estimation – the lattice planes are flat and parallel, (c) wrong estimation of radius – the lattice is distorted.

The radius of curvature of the sample tip (R) and the field factor (*k*-factor) should be defined in a reconstruction. Because the initial tip radius is small, typically around 30 nm, and the top of the tip may be lost before the field evaporation stabilizes, it is difficult to determine R beforehand only from scanning electron microscope (SEM) images. IVAS is equipped with a function to fit the *k*-factor based on changes in the voltage (V) applied to the sample during the APT measurement and the taper

of the sample observed by the SEM before the measurement, as follows: $k = V/(F \cdot R)$, where F is an element-dependent evaporation voltage. The *k*-factor is fitted such that the change in diameter in the z-direction matches the change in specimen voltage. Reconstruction using this method assumes that the initial radius estimation is accurate. The initial radius was determined by the following process:

(1) Assume an appropriate initial radius based on the SEM image, as shown in Fig. 3a.
(2) Estimate the compression factor using the process explained in Section 3.1 and using the Reconstruction Explorer function in IVAS to obtain the reconstructed atomic planes.
(3) Observe the atomic map and identify atomic planes whose normal vector is close to the z-direction in the preview reconstructed image.
(4) If there is any distortion, for instance in the Fig. 3c, increase or decrease the assumed radius and return to step (1). If flat and parallel atomic planes can be obtained as in Fig. 3b, then the assumption of initial radius was acceptable, the quantitative analysis will be continued after doing final reconstruction as described in the next paragraph.

The ICF and initial tip radius values calculated by the method explained in 3.1 and 3.2 were used to reconstruct the 3-D image of the atomic distribution map as shown in Fig. 4. The d-space of (hkl) plane could be determined by using Fast Fourier Transformation (FFT). It was compared with the theoretical value of d_{hkl} in BCC iron structure to confirm the correctness of the reconstruction process. Low index orientation is preferred for calculation because the plane distance is quite large, which facilitates data processing. Herein, the ROI along with <100> direction was extracted to do analysis. When the z-axis of the specimen was close to <100>, the value $d_{200} = 0.141 \pm 0.008$ nm was consistent with the theoretical value of the iron lattice in the BCC structure (unit cell a = 0.286 nm). The d_{200} was calculated at the several regions along with z-axis, but there were no significant differences between top and bottom regions in the specimen.

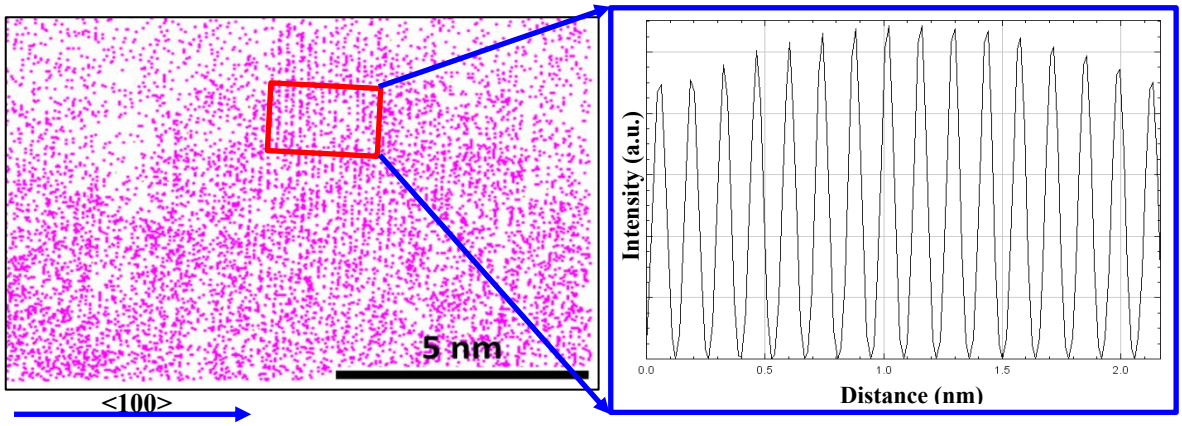

Fig. 4 – Reconstructed image extracted near <100> direction. Fast Fourier transformation was applied on the red rectangle region. In BCC structure, the d-space appeared here is corresponding to d_{200}.

4. Solute Enrichment Analysis

As shown in Fig. 5, the distribution of solute atoms varied greatly depending on the expected aggregation mechanism. Fig. 5a illustrates the isoconcentration surface where the Cu concentration in FeCu is 4%. Although the presence of interstitial loops in iron–copper alloys has been confirmed, there are no reports about the segregation of copper atoms to the loops. Because Cu atoms have a very low solubility limit in BCC iron, they precipitate faster than the dislocation loops develop, forming CRPs that independently precipitate at random locations [27]. Based on the precipitation mechanism, the CRPs were expected to be spherical. However, the isoconcentration surfaces in the three-dimensional image in Fig. 5a show that most of these clusters were ellipsoids with the smaller dimension along the z-axis and nearly identical dimensions along the x- and y-axes. This difference may be the result of variations in the field ion evaporation values. The electric field required for ionization and evaporation of copper(I) is 30 V/nm, while the corresponding value of iron(II) is 33 V/nm [28]. Therefore, the evaporation field of 33 V/nm used for reconstruction should not affect the results of iron atoms. However, it could affect the positions of the copper atoms in the APT results

because of their smaller evaporation field. Copper atoms near the surface may evaporate easier than iron atoms, shortening their distances and causing shrinkage in the three-dimensional map. Compared to that along the x- and y-axes, this change in distance is greater along the z-axis because it is the direction of the electric field used in the APT system. This effect appeared similarly with the so-called "local magnification" caused by surface-induced distortions reported by Vurpillot and Geuser et al. [29],[30]. In contrast, the 3.34% Mn and 2.58% Ni isoconcentration surfaces of the FeMnNi alloy in Fig. 4b show that these solutes tended to cluster as a part of a toroidal shape in specific planes. The special distribution of the Mn and Ni isoconcentration surfaces indicates that these atoms might be attached to the dislocation loops, as reported in Ref. [11].

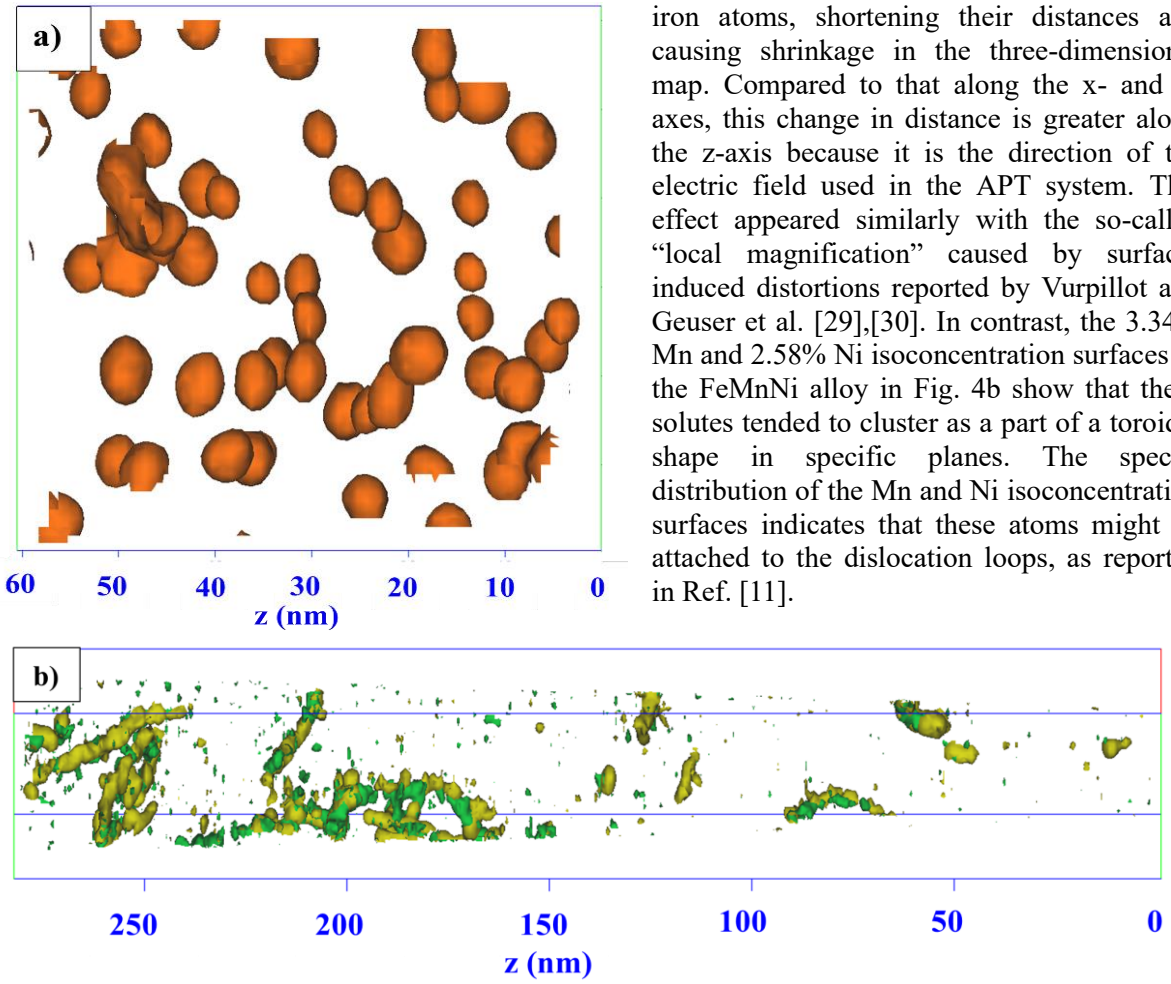

Fig. 5 – Isoconcentration surfaces of solute elements in alloys. (a) In the FeCu alloy, copper clusters (orange) are ellipsoids. (b) In the FeMnNi alloy, areas enriched with manganese (yellow) and nickel (green) form part of a torus.

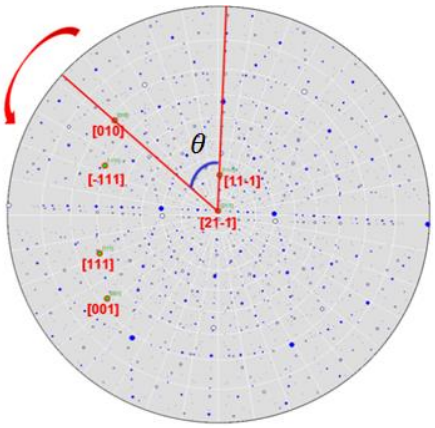

Fig. 6 – Wulff diagram. The center pole corresponds to the [21-1] direction. Using pole [-11-1] as an initial position, the rotation angles (θ) along the z-axis were estimated to determine the candidate plane direction.

To evaluate the orientation of the toroidal enrichment of Mn and Ni, the crystal orientation was identified. First, using the coordinates of polar points from the DI, the crystal orientation of the specimen in the z-direction was determined. According to the Wulff diagram analysis shown in Fig. 6,

the z- and y-axes of the specimen in Fig. 5b were very close to the [21-1] and [-11-1] directions, respectively. Then, the toroidal plane was clarified by choosing the criteria for the isoconcentration surface. As shown in Fig. 7, by rotating the isoconcentration surface map along the z-axis, the angle at which the toroidal surface looked like a line was found. The actual angles (φ) between the z-axis and the normal vector of the solute-enriched planes were calculated. Similarly, by rotating the atom map along with the y-axis, the angles between the y-axis and the solute-enriched planes were defined.

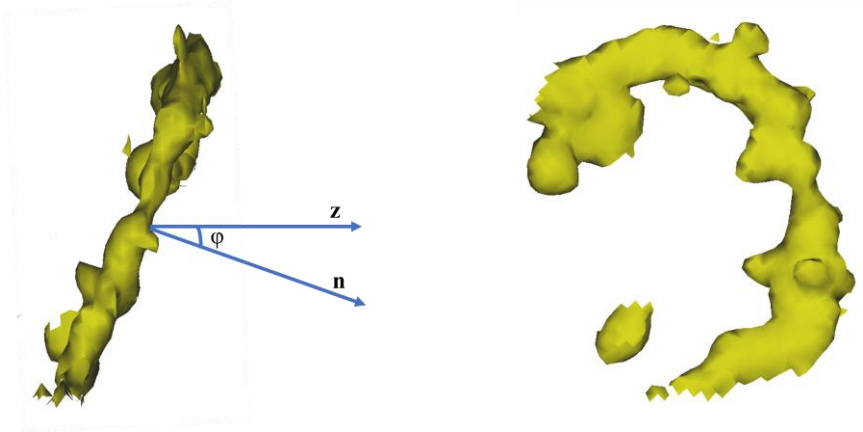

Fig. 7 – Manganese decoration on the edge of a dislocation loop. The side-view (left) and front-view (right) of the manganese isoconcentration surface show that there was no elongation or distortion in the spatial position of solute atoms.

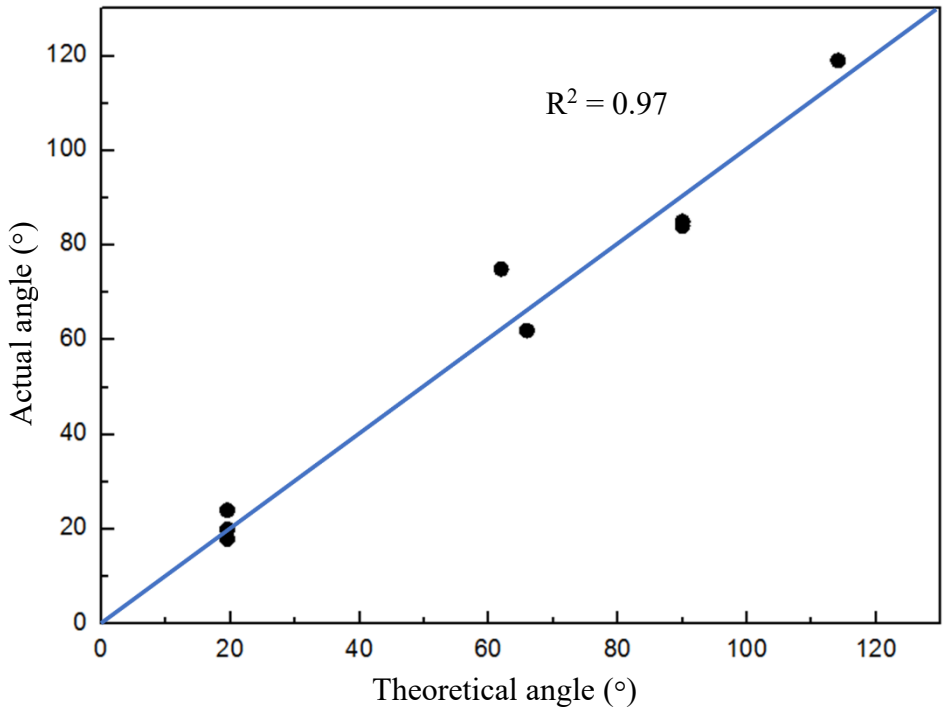

Fig. 8 – Correlation between the measured angle φ (y-axis) and the interplanar angle φ' (x-axis). Relationships between φ values and φ' values are represented by nine black dots. The plot of the (y = x) line is in blue color.

In this experiment, because two types of loops (100) and (111) were confirmed in our previous work [31], the corresponding angles (φ') between the z-axis ([21-1] direction) and the (111) and (100) crystallographic planes were calculated using equation (1) and compared with the measured angles (φ). The interplanar angle φ' between ($h_1k_1l_1$) and ($h_2k_2l_2$) for the cubic system was calculated using the following equation:

$$\cos\varphi' = \frac{h_1h_2+k_1k_2+l_1l_2}{\sqrt{(h_1^2+k_1^2+l_1^2)(h_2^2+k_2^2+l_2^2)}} \qquad (2)$$

Note that in this three-dimensional image, only the absolute value of the empirical angle φ between the z-axis and the normal of the plane containing the enriched solute $|\varphi| < 90°$ can be determined, and equation (2) provides the theoretical angle between 0° and 180°. To synchronize these two results, we converted the theoretical results with values greater than 90° into corresponding negative values. When the nine solute-enriched planes identified in Fig. 5b were assigned to the orientation of the dislocation loop with the closest angle, two were determined to be of type $\boldsymbol{b}$ = <100> and seven of type $\boldsymbol{b}$ = 1/2<111>. The appearance of two types of dislocation loops, in which the fraction of <111> type is larger than that of <100> type, is consistent with the results of previous studies [31]. Fig. 8 shows the correlation between the measured angle φ and the theoretical angle φ'. The two are in good agreement, which confirms that the proposed method can reasonably extract the crystallographic features of solute atoms segregated on a plane using only the APT desorption images.

5. Conclusion

In this study, a method to improve the APT reconstruction of iron model alloys was proposed and successfully implemented, and the irradiation-induced microstructures of FeCu and FeMnNi were analyzed. Accordingly, the matrix atoms did not change their spatial position, while a thick region of minority elements, such as a copper cluster, shrunk along the z-direction owing to differences in the evaporation field. Mn and Ni atoms exhibited a different behavior, in which they segregated to the edge of dislocation loops to form a toroidal enriched region. In addition, the orientation of planar objects comprising solute decoration of dislocation loops was calculated in detail. Three basic steps are required, as follows. First, the specimen must be carefully prepared to optimize the calculation process and reduce errors caused by lattice distortion due to the existence of solute atoms in the alloy as well as by lattice defects generated by irradiation. Depending on the experimental and sample conditions, either a specimen coupon or a needle tip is selected. Second, the reconstruction parameters are estimated. Initially, the poles on the desorption map must be identified using crystal orientation analysis. When more poles are identified on the detector hit map, the calculated orientation of the specimen is more accurate. Confirmation of whether the specimen contains one or more grains should also be performed in this step. The ICF value is determined after comparing the results from crystal orientation analysis and the data obtained from manual calculations, while the radius of curvature is calculated based on the SEM image and the applied voltage history. Finally, candidate orientations are selected based on the comparison between theoretical and experimental interplanar angles, and the orientations are confirmed by rotation along the z-direction, if necessary.

Acknowledgements

This work was partially supported by the Japan Society for the Promotion of Science (JSPS) KAKENHI [grant 19K22153].

References

[1] M. K. Miller, K. F. Russell, J. Kocik, and E. Keilova, "Embrittlement of low copper VVER 440 surveillance samples neutron-irradiated to high fluences," *J. Nucl. Mater.*, vol. 282, no. 1, pp. 83–88, 2000.

[2] M. K. Miller, K. A. Powers, R. K. Nanstad, and P. Efsing, "Atom probe tomography characterizations of high nickel, low copper surveillance RPV welds irradiated to high fluences," *J. Nucl. Mater.*, vol. 437, no. 1–3, pp. 107–115, 2013.

[3] K. Murakami, "Influence of copper precipitates on clustering behavior of alloying elements observed in Japanese reactor pressure vessel surveillance materials using atom probe tomography," *J. Nucl. Mater.*, vol. 542, 2020.

[4] A. Wagner, A. Ulbricht, F. Bergner, and E. Altstadt, "Influence of the copper impurity level on

the irradiation response of reactor pressure vessel steels investigated by SANS," *Nucl. Instruments Methods Phys. Res. Sect. B Beam Interact. with Mater. Atoms*, vol. 280, pp. 98–102, 2012.
[5] P. D. Styman, J. M. Hyde, K. Wilford, A. Morley, and G. D. W. Smith, "Precipitation in long term thermally aged high copper, high nickel model RPV steel welds," *Prog. Nucl. Energy*, vol. 57, pp. 86–92, 2012.
[6] P. B. Wells *et al.*, "Evolution of manganese-nickel-silicon-dominated phases in highly irradiated reactor pressure vessel steels," *Acta Mater.*, vol. 80, pp. 205–219, 2014.
[7] B. C. Masters, "Dislocation loops in irradiated iron [3]," *Nature*, vol. 200, no. 4903, p. 254, 1963.
[8] B. L. Eyre and R. Bullough, "On the formation of interstitial loops in b.c.c. metals," *Philos. Mag.*, vol. 12, no. 115, pp. 31–39, 1965.
[9] J. H. Ke, H. Ke, G. R. Odette, and D. Morgan, "Cluster dynamics modeling of Mn-Ni-Si precipitates in ferritic-martensitic steel under irradiation," *J. Nucl. Mater.*, 2018.
[10] K. Yabuuchi, R. Kasada, and A. Kimura, "Effect of Mn addition on one-dimensional migration of dislocation loops in body-centered cubic Fe," *Acta Mater.*, vol. 61, no. 17, pp. 6517–6523, 2013.
[11]E. Meslin, B. Radiguet, and M. Loyer-Prost, "Radiation-induced precipitation in a ferritic model alloy: An experimental and theoretical study," *Acta Mater.*, vol. 61, no. 16, pp. 6246–6254, 2013.
[12] M. Herbig, D. Raabe, Y. J. Li, P. Choi, S. Zaefferer, and S. Goto, "Atomic-scale quantification of grain boundary segregation in nanocrystalline material," *Phys. Rev. Lett.*, vol. 112, no. 12, pp. 1–5, 2013.
[13] G. R. Odette, T. Yamamoto, T. J. Williams, R. K. Nanstad, and C. A. English, "On the history and status of reactor pressure vessel steel ductile to brittle transition temperature shift prediction models," *J. Nucl. Mater.*, vol. 526, p. 151863, 2019.
[14] K. Y. Xie *et al.*, "Breaking the icosahedra in boron carbide," *Proc. Natl. Acad. Sci. U. S. A.*, vol. 113, no. 43, pp. 12012–12016, 2016.
[15] M. P. Moody *et al.*, "Lattice rectification in atom probe tomography: Toward true three-dimensional atomic microscopy," *Microsc. Microanal.*, vol. 17, no. 2, pp. 226–239, 2011.
[16] P. J. Warren, A. Cerezo, and G. D. W. Smith, "Observation of atomic planes in 3DAP analysis," *Ultramicroscopy*, vol. 73, no. 1–4, pp. 261–266, 1998.
[17] L. T. Belkacemi, E. Meslin, J. P. Crocombette, B. Radiguet, F. Leprêtre, and B. Décamps, "Striking effect of solute elements (Mn, Ni) on radiation-induced segregation/precipitation in iron-based model alloys," *J. Nucl. Mater.*, vol. 548, 2021.
[18] M. Wechsler and R. Berggren, "Reactor Pressure-Vessel Materials," *Nucl. Saf.*, vol. Vol: 5, 1964.
[19] H. W. King, "Quantitative size-factors for metallic solid solutions," *J. Mater. Sci.*, vol. 1, no. 1, pp. 79–90, 1966.
[20] T. F. Kelly and M. K. Miller, "Invited review article: Atom probe tomography," *Rev. Sci. Instrum.*, vol. 78, no. 3, 2007.
[21] B. Gault, F. De Geuser, L. T. Stephenson, M. P. Moody, B. C. Muddle, and S. P. Ringer, "Estimation of the reconstruction parameters for atom probe tomography," *Microsc. Microanal.*, vol. 14, no. 4, pp. 296–305, 2008.
[22] K. Murakami, T. Iwai, H. Abe, and N. Sekimura, "Improvement of the High Fluence Irradiation Facility at the University of Tokyo," *Nucl. Instruments Methods Phys. Res. Sect. B Beam Interact. with Mater. Atoms*, vol. 381, pp. 67–71, 2016.
[23] J. F. Ziegler, M. D. Ziegler, and J. P. Biersack, "SRIM - The stopping and range of ions in matter (2010)," *Nucl. Instruments Methods Phys. Res. Sect. B Beam Interact. with Mater. Atoms*, vol. 268, no. 11–12, pp. 1818–1823, 2010.
[24] B. L. Adams, S. I. Wright, and K. Kunze, "Orientation imaging: The emergence of a new microscopy," *Metall. Trans. A*, vol. 24, no. 4, pp. 819–831, 1993.
[25] CAMECA, "IVAS™ 3.8.0 User Guide," 2017.
[26] Y. Chen *et al.*, "Automated Crystallographic Identification of Atom Probe's Ion Desorption Map," *Microsc. Microanal.*, vol. 23, no. S1, pp. 662–663, 2017.
[27] T. Kudo, R. Kasada, A. Kimura, K. Hono, K. Fukuya, and H. Matsui, "Factors Controlling

Irradiation Hardening of Iron-Copper Model Alloy," *Mater. Trans.*, vol. 45, no. 2, pp. 338–341, 2004.
[28] T. T. Tsong, "Field ion image formation," *Surf. Sci.*, vol. 70, no. 1, pp. 211–233, 1978.
[29] F. Vurpillot, A. Bostel, E. Cadel, and D. Blavette, "The spatial resolution of 3D atom probe in the investigation of single-phase materials," *Ultramicroscopy*, vol. 84, no. 3, pp. 213–224, 2000.
[30] F. De Geuser, B. Gault, A. Bostel, and F. Vurpillot, "Correlated field evaporation as seen by atom probe tomography," *Surf. Sci.*, vol. 601, no. 2, pp. 536–543, 2007.
[31] P. Prak Tom, K. Murakami, V. N. Luu, B. V. C. Nguyen, and L. Chen, "Effect of solute elements (Ni, Mn) in Fe-based alloys on dislocation loop evolution under Fe2+ ion irradiation," *J. Nucl. Mater.*, vol. 559, p. 153489, 2022.